A&A 432, 475–489 (2005)
DOI: 10.1051/0004-6361:20041671

Astronomy & Astrophysics

Neutral hydrogen gas in 7 high-inclination spiral galaxies

I. The data⋆

M. Dahlem[1], M. Ehle[2], S. D. Ryder[3], M. Vlajić[4], and R. F. Haynes[5]

[1] CSIRO/ATNF Paul Wild Observatory, Locked Bag 194, Narrabri NSW 2390, Australia
e-mail: Michael.Dahlem@csiro.au
[2] XMM-Newton Science Operations Centre, European Space Agency, Apartado 50727, Villafranca del Castillo, 28080 Madrid, Spain
[3] Anglo-Australian Observatory, PO Box 296, Epping NSW 1710, Australia
[4] Department of Astronomy, Faculty of Mathematics, University of Belgrade, Studentski Trg 16, 11000 Belgrade, Serbia and Montenegro
[5] School of Mathematics & Physics, University of Tasmania, GPO Box 252-37, Hobart 7001, Tasmania, Australia

Received 16 July 2004 / Accepted 16 November 2004

Abstract. High-sensitivity interferometric H I line observations of a small sample of seven galaxies with limiting column densities of a few times 10^{19} cm^{-2} are presented. A tilted ring model fitting routine was used to determine some global characteristics of the H I distribution and kinematics in the galaxy disks. 4 of the 7 galaxies have low maximum rotation velocities of $\lesssim$125 km s^{-1}, indicating that they are low-mass systems. Visual inspection shows that at least one galaxy, NGC 4700, exhibits signs of extraplanar H I emission. An in-depth search for H I gas in the galaxy halos and the determination of halo gas properties, based on three-dimensional modeling, will follow in a separate publication. Companion galaxies were detected in H I line emission near 3 of the 7 sample galaxies: NGC 1511, NGC 4565 and NGC 4700. One of these, NGC 1511, is found to be strongly interacting and is therefore not suitable for a study of the dependence of its halo properties on the level of star formation activity in the underlying disk. In the case of NGC 4700 the companion galaxy has no visible influence on its gas kinematics, while NGC 4565 might be affected by its interaction with two small companions.

Key words. ISM: general – galaxies: ISM – galaxies: evolution – galaxies: halos – galaxies: starburst – galaxies: kinematics and dynamics

1. Introduction

Observations of the hyperfine transition of neutral hydrogen, H I, with a rest frequency of 1420.405 MHz, of galaxies have been conducted for four decades, leading to our current level of understanding of the distribution and kinematics of atomic gas in galaxies, including the Milky Way. Large single-dish H I surveys (e.g. Mathewson et al. 1992), most recently the H I Parkes Sky Survey (HIPASS; Barnes et al. 2001; Meyer et al. 2004), provide us with total H I emission spectra of thousands of galaxies. More detailed information is derived from interferometric H I line observations of external galaxies, as done e.g. in the Westerbork observations of neutral hydrogen in irregular and spiral galaxies (WHISP; Swaters et al. 2002a,b, and references therein).

H I line studies are the best means of detecting gas in galaxies far away from their centres. The radial extent of the H I distribution of many galaxies is several times larger than their optical extent (e.g. NGC 628, Kamphuis & Briggs 1992; Circinus, Jones et al. 1999). H I emission also traces gas plumes and bridges in interacting systems, such as e.g. the Leo triplet (Haynes et al. 1979; Wilding et al. 1993) and the NGC 4631 group of galaxies (Combes 1978; Rand & Stone 1996). In addition, H I observations have led to the detection that the Milky Way has not only a thin neutral atomic gas disk, but a second H I gas component, with higher velocity dispersion (σ = 60 km s^{-1}), an exponential scale height of z_0 = 4.4 kpc and a projected vertical column density of 1.4 × 10^{19} cm^{-2}, see Kalberla et al. (1998) and references therein. Despite early searches of gaseous halos around spiral galaxies, e.g. in M 31 (e.g. Kraus & Dixon 1967), the first detection of halo emission was made only 10 years later in NGC 4631 (Ekers & Sancisi 1977). Considering cosmic-ray electrons to be part of a generalised ISM, one might consider this the first detection of a gaseous halo. The first bona fide detection of an H I gas halo in a non-interacting external galaxy was reported yet 20 years later, by Swaters et al. (1997), who imaged the edge-on spiral galaxy NGC 891 with unprecedented sensitivity. Since then

⋆ Figures 1, 5, 6, 10, 14, 15, 19, 20, 24, 28 and Appendix A are only available in electronic form at http://www.edpsciences.org

the detection of extraplanar H I has been reported in only a few cases, such as NGC 2403 (Fraternali et al. 2002), the most recent observations of NGC 891, detecting H I up to z-distances of 15 kpc (Fraternali 2003, 2004), NGC 2613 (Irwin & Chaves 2003, and references therein), UGC 7321 (Matthews & Wood 2003) and most recently NGC 253 (Boomsma et al. 2005). This proves that H I observations are also suitable to trace neutral atomic gas in the halos of spiral galaxies.

Thus, H I observations have been established as a very powerful means of tracing low surface brightness gas far away from the centres of galaxies.

Here we present the results from our high-sensitivity H I line observations to search for low surface brightness atomic gas in a small sample of 7 highly inclined galaxies with different star formation (SF) rates. The observations were conducted with three of the most powerful centimetre wavelength radio interferometers, namely the Australia Telescope Compact Array (ATCA[1]), the Very Large Array (VLA[2]) and the Westerbork Synthesis Radio Telescope (WSRT[3]). The required sensitivity was reached with these telescopes by coadding multi-configuration data, using state-of-the-art cooled 1.4-GHz receivers and in the case of the WSRT its new wideband correlator.

In the present study we concentrate on presenting our data base and quantifying first the properties of the H I gas in the galaxy disks. A detailed description of the low surface brightness gas around the target galaxies will be presented separately. In particular, the data will be used to study the dependence of gaseous halos' properties on the distribution and level of star-forming activity in the underlying disk. Section 2 describes the observations and data reduction. The results are presented in Sect. 3, followed by a short discussion in Sect. 4.

2. Observations and data reduction

2.1. ATCA observations

The galaxies observed by us with the ATCA are NGC 1511, NGC 7090 and NGC 7462. Each was observed with one compact array configuration (375 m array or equivalent) and different configurations of the 750 m and 1.5 km arrays, as well as at least one 6 km configuration, to obtain good angular resolution; see Table 1. The individual observing runs were normally 11−13 h long (including time for calibration), providing almost full 12 h aperture syntheses in each configuration. The total on-source integration times are 73.3 h (NGC 1511), 59.6 h (NGC 7090) and 54.8 h (NGC 7462). These are amongst the most sensitive H I observations conducted with the ATCA so far.

[1] The Australia Telescope is funded by the Commonwealth of Australia for operation as a National Facility managed by CSIRO.

[2] The National Radio Astronomy Observatory (NRAO) is a facility of the National Science Foundation operated under cooperative agreement by Associated Universities, Inc.

[3] The Westerbork Synthesis Radio Telescope is operated by ASTRON (the Netherlands Foundation for Research in Astronomy) with support from the Netherlands Foundation for Scientific Research (NWO).

Table 1. ATCA observation details.

Galaxy	Array[a]	Date
NGC 1511	375[b]	1995, Aug. 08
	750A	2002, Jan. 06
	750D	2003, Feb. 26
	1.5A[b]	1995, Mar. 24
	1.5B	2003, Jan. 13
	1.5D	2001, Nov. 18
	6A	2003, Mar. 06
NGC 7090	352	2001, Oct. 14
	750D	2003, Feb. 24
	1.5B	2003, Jan. 14
	1.5D	2001, Nov. 16
	6D	2003, July 15
	6A	2003, Dec. 14
NGC 7462	352	2001, Oct. 16
	750D	2001, Sep. 27
	1.5B	2003, Jan. 15
	1.5D	2001, Nov. 20
	6D	2003, July 16
	6A	2003, Dec. 13

Notes:
[a] The ATCA is operated in configurations with maximum baselines ranging from 75 m to 6 km. For 750-m, 1.5-km and 6-km configurations, 4 subsets (A,B,C,D) each exist.
[b] The 1995 data of NGC 1511 were retrieved from the public ATCA data archive.

Simultaneously, the 1.39 GHz continuum of the target galaxies was also imaged by us in the second IF (Intermediate Frequency). These data are used to improve the sensitivity, uv-coverage and angular resolution of the data presented by us earlier (Dahlem et al. 2001). These new images will be mentioned only briefly in Appendix A.

1934-638 was used as the primary flux and bandpass calibrator, 0252-712 (for NGC 1511) and 2117-642 (for NGC 7090) and 2311-452 (for NGC 7462) as phase calibrators. The adopted flux of 1934-638 is 14.94 Jy at 1.43 GHz. The data reduction was performed in a standard fashion, using the software package MIRIAD.

Standard data reduction was performed (cf. Miriad User's Guide) and the underlying radio continuum was subtracted from the H I line data in the uv-plane.

With angular extents of their radio emission of $\lesssim 4'$ (see below), NGC 7090 and NGC 7462 are so small that they fit easily into the primary beam of the ATCA's 22-m antennae (Full Width at Half Maximum $FWHM = 34'$ at 1.43 GHz) and no primary beam correction is necessary.

Since for NGC 1511 archival data with a different pointing centre were used by us in conjunction with our own observations, images were produced in mosaic mode. In this process a primary beam correction is applied automatically in miriad (using the tasks invert and mossdi). In the case of NGC 1511 and its companions this turned out to be necessary, due to an unexpectedly extended distribution of H I emission (see Sect. 3).

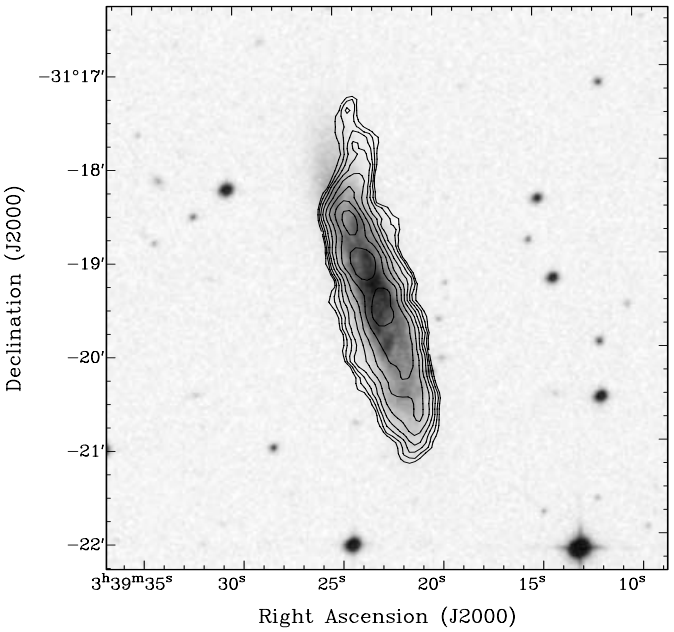

Fig. 2. NGC 1406 overlay of HI total intensity map on DSS-2 red optical image. The FOV is 6′ × 6′ (26 kpc × 26 kpc). Contours are at the 0.25 (=1.6 × 10^{21} cm^{-2}), 0.35, 0.5, ... 2.8 Jy km s^{-1} surface brightness levels, separated by factors of $\sqrt{2}$.

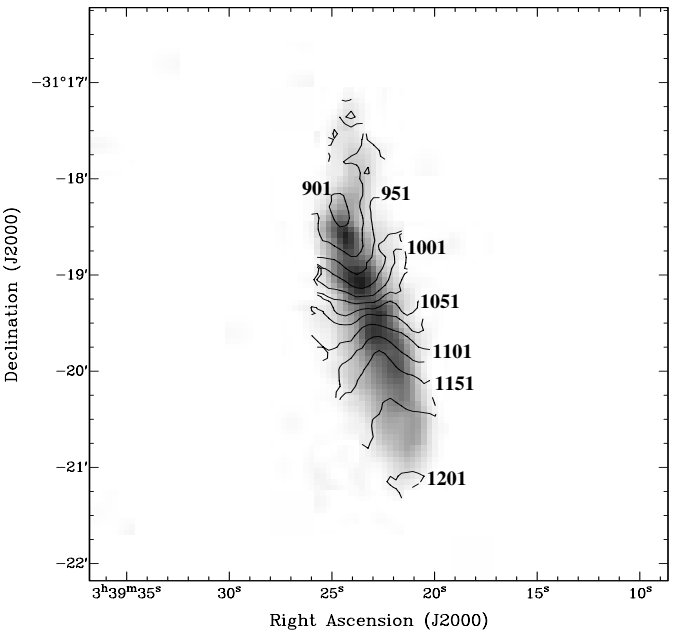

Fig. 3. NGC 1406 HI velocity field overlaid on HI total intensity image. The FOV is the same as in Fig. 2. The contours display the galaxy's systemic velocity of 1051 km s^{-1} ± (n × 25) km s^{-1}, ranging from 901 km s^{-1} to 1201 km s^{-1}.

The original channel width of the data is 1.65 km s^{-1}; in order to further improve the signal-to-noise of the data, this was reduced offline to 4.95 km s^{-1}. It is also not practical for searches for low surface brightness emission to leave the data at their original angular resolution of about 6″. Instead, tapered data are presented here, with reduced angular resolution (robust = 0.5 weighting).

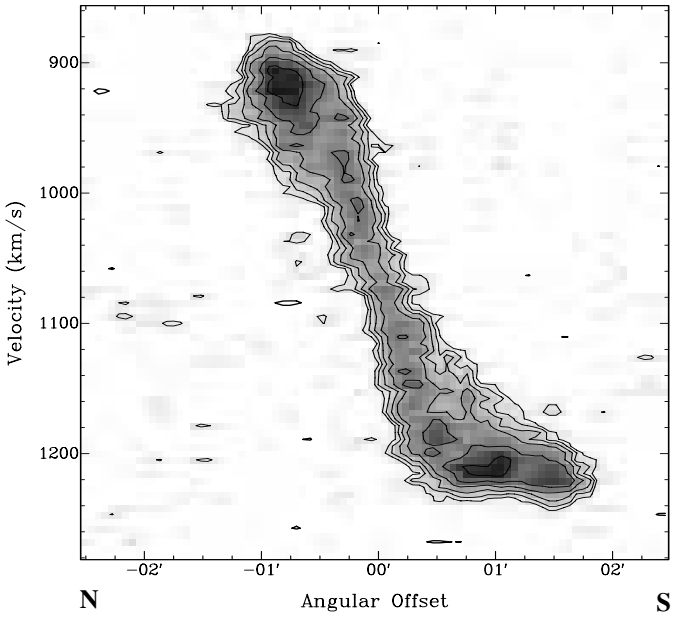

Fig. 4. NGC 1406 *pv* diagram along the major axis, covering a radial range of ±2.′5 (±10.8 kpc). Contours show surface brightness levels of −7, 7 (=2.5-σ), 10, 14, ..., 40 mJy beam^{-1}, separated by factors of $\sqrt{2}$. Negative contours are bold.

Table 2. VLA observation details.

Galaxy	Array	Date
NGC 1406	CnB	2002, Sep. 26
NGC 4666[a]	C	1997, June 24–26
	D	1996, Aug. 13
NGC 4700	C	2002, Dec. 13

Note:
[a] Walter et al. (2004).

2.2. VLA data

NGC 1406 and NGC 4700 were observed with the VLA, in 4IF mode, for 4:37 h and 6:40 h, respectively (Table 2). The original channel width of the data is 5.2 km s^{-1}. For NGC 1406 3C 48 was used for flux and bandpass calibration and 0416-188 as phase calibrator. For NGC 4700 we used 3C 286 and 1246-075, respectively. In the new default configuration of the VLA's C array ("CS"), with very short baselines in its central part, losses of extended flux at 1.42 GHz are negligible.

Data reduction was carried out in the standard fashion, using the AIPS software package (cf. AIPS Cookbook) by the National Radio Astronomy Observatory (NRAO). Continuum subtraction was performed using the task UVBAS, subtracting the visually pre-selected line-free channels. Images were created using robust = 0.5 weighting, which offers a good compromise between angular resolution and sensitivity.

From the line-free channels narrow-band continuum images were produced, of which we present the one of NGC 4700 in Appendix A.

Table 3. WSRT observation details.

Galaxy	Array[a]	Date
NGC 4244	36	2003, Feb. 13
	54	2003, Feb. 19
	72	2003, Feb. 20
	90	2003, Apr. 13
NGC 4565	36	2003, Feb. 16
	54	2003, Apr. 14
	72	2003, May 14
	90	2003, May 19

Note:
[a] The so-called "traditional" array configuration was used in all cases (see WSRT documentation for details). We list here the shortest RT9−RTA baselines of the four configurations that the traditional array configuration comprises.

Table 4. Parameters of the data cubes.

Galaxy	Channel	Ang. Res.	rms Noise	
	Width (km s^{-1})	($''$)	(10^{19} cm^{-2})	(mJy/beam)
NGC 1406	5.18	$15\farcs0 \times 12\farcs0$	9.12	2.75
NGC 1511	4.95	$21\farcs8 \times 17\farcs3$	1.62	1.07
NGC 4244	8.24	$17\farcs8 \times 11\farcs2$	1.66	0.35
NGC 4565	8.24	$26\farcs0 \times 10\farcs7$	1.09	0.32
NGC 4666	5.18	$18\farcs7 \times 16\farcs2$	0.77[a]	0.39[a]
NGC 4700	5.18	$20\farcs0 \times 15\farcs0$	1.13	0.57
NGC 7090	4.95	$20\farcs0 \times 15\farcs0$	1.92	0.92
NGC 7462	4.95	$22\farcs1 \times 13\farcs6$	2.20	1.16

Note:
[a] From Walter et al. (2004).

2.2.1. Earlier observations

In the context of this investigation also results from H I observations of the edge-on starburst galaxy NGC 4666 (Walter et al. 2004) are relevant, which brings the total number of suitable datasets for the search to 8. However, in NGC 4666 no conclusive evidence for the existence of H I gas in its halo was detected (for details see Walter et al. 2004).

2.3. WSRT observations

Two nearby edge-on spiral galaxies, NGC 4244 and NGC 4565, were observed by us with the WSRT, using its so-called "traditional" array configuration, as outlined in Table 3. Using the 1024-channel correlator mode, the original channel width of the data is 2.1 km s^{-1}. Flux and bandpass calibration was performed by observing either 3C 48 or 3C 147 during each 12-h observing run. The on-source integration time is 47.5 h per galaxy.

The data were reduced using MIRIAD, with adapted tasks for WSRT data, following the standard procedure for WSRT data reductions, which makes use of post-observation self-calibration instead of phase calibrator observations to focus the array. Continuum subtraction was performed in the uv-plane and the gain and phase solutions of the self-calibrated continuum data subsequently applied to the H I line data (WSRT Guide, Chap. 9). Then the data from the different configurations were co-added into a single uv-dataset and cleaned and imaged.

A correction for primary beam attenuation was applied, because both objects are large compared to the WSRT's 30′ primary beam.

3. Results

Different final H I datacubes were created for each galaxy. Here we present only the versions created with a "robust" factor of 0.5 for the ATCA and VLA, which offers a near-optimal compromise between angular resolution and sensitivity, and of −0.5 for the WSRT, which provides optimal grating ring suppression. The sampling interval (pixel size) of the H I datasets presented here is 4″ (except for NGC 1406, where a pixel size of $3\farcs5$ was chosen).

Cleaning of the channel maps was performed only in areas around emission features, using smoothed versions of the datacubes to create masks defining the clean regions. The smoothed cubes have angular resolutions of 1.5 times those of the restored beam of the original data; the 3-σ confidence level in the channel maps of the smoothed datacubes was used to mark the regions that were cleaned.

Moment maps were produced from the cubes of the cleaned data. The zeroeth moment map represents the total H I emission distribution, the first moment is the galaxies' velocity field. We do not present here images of the second moment (i.e. the H I velocity dispersion along each line of sight). The same masks that were defined for cleaning (the 3-σ confidence level in the channel maps of the smoothed datacubes) were then used to select the regions from which the moment maps were created.

After a basic kinematic analysis of each object (Sect. 3.8), position-velocity (*pv*) diagrams were produced along the galaxies' major axes.

For each of the galaxies observed by us we present here the following graphical displays:

1. H I channel maps with a channel width of 15−17 km s^{-1};
2. maps of the H I total intensity distribution, overlaid on second generation Digital Sky Survey (DSS-2) red images;
3. H I velocity fields, overlaid as contours on grey-scale reproductions of the total intensity maps;
4. H I position-velocity (*pv*) diagrams along the major axes.

In some cases new 1.4 GHz radio continuum images are presented in Appendix A.

The long integrations mentioned above led to high sensitivity of the data. The angular resolutions, channel widths and single velocity channel 1-σ rms noise of our datasets are listed in Table 4. In the following subsections a brief description of

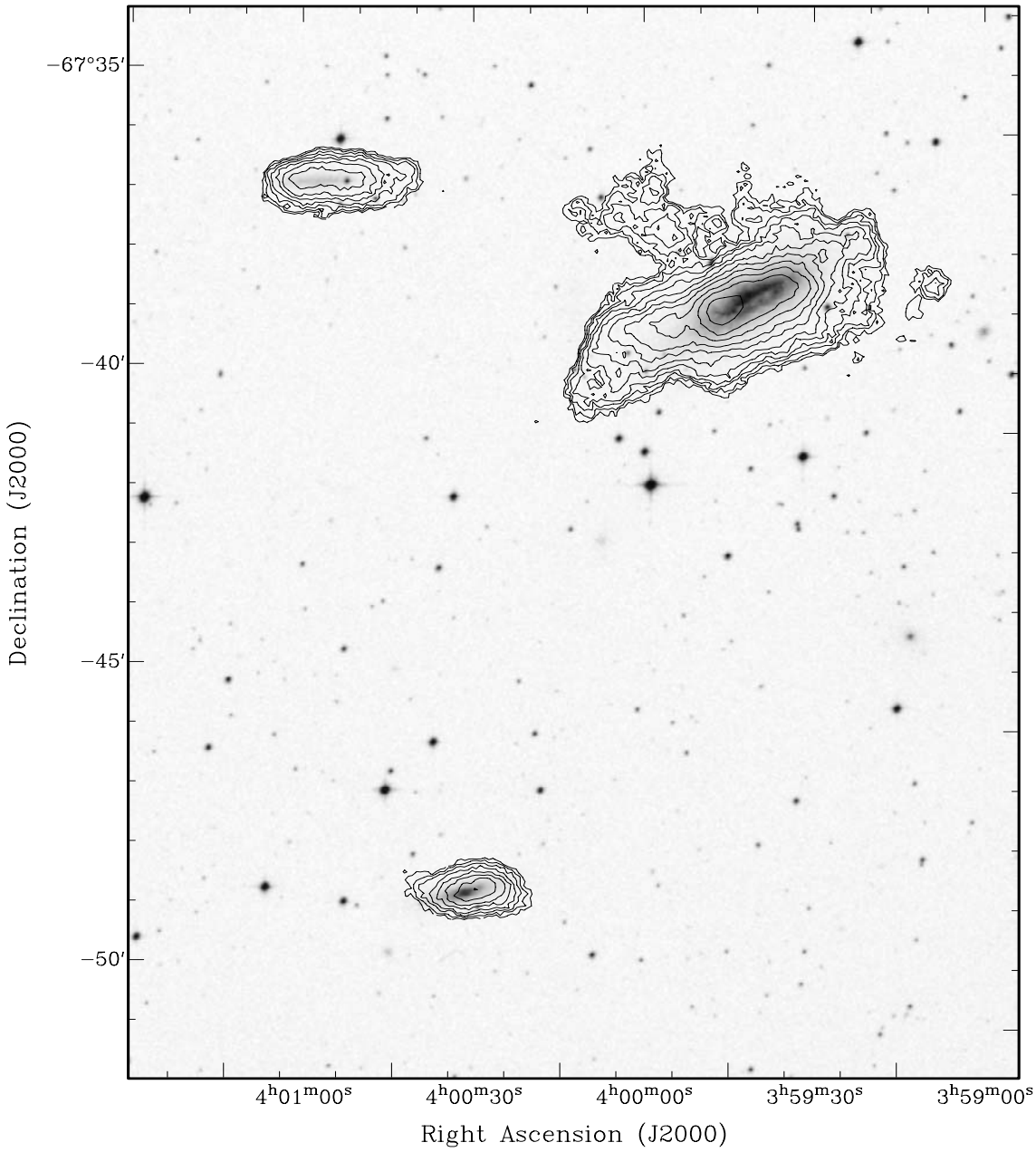

Fig. 7. NGC 1511 group overlay of HI total intensity map on DSS-2 red optical image. The FOV is 15′ × 18′ (76.4 kpc × 91.7 kpc). Contours are at the 0.05 (=1.5 × 10^{20} cm^{-2}), 0.07, 0.1, ..., 1.6 Jy km s^{-1} surface brightness levels, separated by factors of $\sqrt{2}$.

our results for each galaxy is given, followed by a summary of the salient H I emission properties.

3.1. NGC 1406

The distribution of H I gas in NGC 1406 (Figs. 1 and 2) is found to follow the optically visible disk, except for its northern part, where the distribution of H I is clearly warped. The detected H I warp has no optical counterpart in the DSS-2 image, down to a limiting magnitude of about 22.0 mag arcsec^{-2}. This warp roots in the inner disk, rather than its northern end, which can be seen in the channel maps at 911–1005.5 km s^{-1} in Fig. 1. There is no sign of a partner galaxy within the field of view of our observations that might explain this disturbance. The radial extent of the H I gas disk in NGC 1406 corresponds to that of its optical disk.

The H I velocity field, which is slightly lop-sided in the central disk, is also disturbed in the northern warp (Fig. 3). In the major axis *pv* diagram in Fig. 4 this disturbance is reflected in an apparent cutoff in the radial H I distribution in the northern half, at a radius of about 75″ (5.4 kpc), while the southern half of the disk extends out to about 110″ (7.9 kpc). The gas at velocities near 900 km s^{-1} missing from the northern half of NGC 1406 in the *pv* diagram is offset from the major axis, in the warp.

NGC 1406 is the strongest continuum source in our small sample, with a 1.4 GHz continuum flux density of 127 ± 7 mJy, which might cause some of the H I to go into absorption against

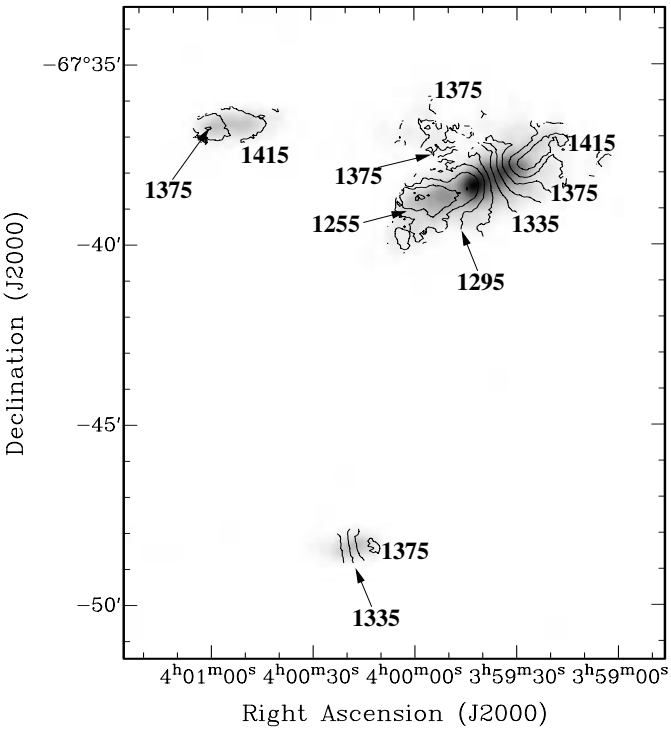

Fig. 8. HI velocity field of the NGC 1511 group, overlaid on our HI total intensity image. The FOV is the same as in Fig. 7. The contours display the galaxy's systemic velocity of 1335 km s^{-1} ± ($n \times 20$) km s^{-1}, ranging from 1255 km s^{-1} to 1415 km s^{-1}.

the brightest continuum emission in the nuclear region and thus lead to an underestimate of the total H I gas mass.

3.2. NGC 1511

Our data show that NGC 1511 is a member of a small group with at least two dwarf companions, NGC 1511a and NGC 1511b (see Figs. 5 and 6). A bridge of H I gas from NGC 1511 to NGC 1511b can be traced with a continuous run in recession velocities in our H I channel maps from about 1340 km s^{-1} to 1400 km s^{-1} (Fig. 5).

Figure 7 shows that the H I gas distribution of NGC 1511 is more extended than the optically visible galaxy in all directions. In addition to this, more H I gas is found in tidally disturbed areas, such as the bridge towards its companion galaxy NGC 1511b (Figs. 6 and 7).

The inner parts of NGC 1511's velocity field (Fig. 8) are quite undisturbed, while further out kinematic disturbances, possibly caused by its two partners, are found. The kinematic disturbances are most prominent in the *pv* diagram displayed in Fig. 9. The velocity field of NGC 1511a (to the south of NGC 1511) is regular; that of NGC 1511b is clearly disturbed, as if the gas was pulled towards NGC 1511. The basic properties of both companion galaxies are described in Sect. 3.8.1.

Unfortunately, the peculiarities arising from the tidal interactions render NGC 1511 unsuitable as target galaxy to study the dependence of its gaseous halo's properties on the distribution and level of star-forming activity in the underlying disk (which was the initial goal of this investigation).

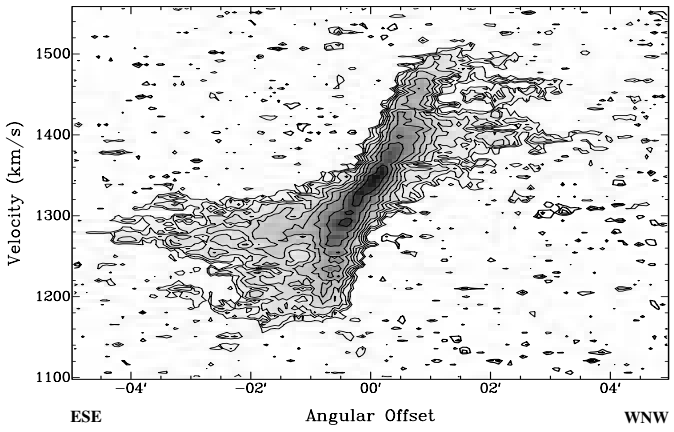

Fig. 9. NGC 1511 *pv* diagram along the major axis, covering a radial range of ±5′ (±25.5 kpc). Contours show surface brightness levels of −2.8, −2, −1.4, 1.4 (=2.5-σ), 2, 2.8, ..., 22.4 mJy beam^{-1}, separated by factors of $\sqrt{2}$. Negative contours are bold.

3.3. NGC 4244

The H I gas distribution in NGC 4244 displayed in Figs. 10 and 11 is mostly regular, with minor disturbances, such as a depression about 4′ northeast of the centre. The kinematics of H I in NGC 4244 is also quite regular, as can be seen in Figs. 10 and 12. Some peculiar features can be discerned in the *pv* diagram (Fig. 13), near the turnover points of galactic rotation. These results are in agreement with earlier observations by Olling (1996a,b). The regularity of NGC 4244 and its quiescence in terms of SF activity might be related to its isolation in space. No partner galaxy or H I cloud was found down to an H I detection limit of order 10^7 $M_\odot$.

3.4. NGC 4565

The northwestern end of the disk of NGC 4565 is strongly warped and there is an indication of a weaker warp also at the southeastern end of the disk (see channel maps in Figs. 14−15). Figure 16 presents the distribution of H I gas in NGC 4565. Except for the outer warp it is mostly undisturbed, with a slight central depression. The warp might be related to the presence of two nearby dwarf companions, most notably one to the north of NGC 4565 (at a projected distance of only ca. 4′ [11.3 kpc] from its disk). The influence of these companions on the behaviour of NGC 4565's H I gas will be investigated in detail by van der Hulst et al. (in prep.). A first report was given by van der Hulst (2004). The slightly disturbed velocity field of NGC 4565 is displayed in Fig. 17. Deviations from regular rotation are not only observed in the warped outer parts of the disk, but the iso-velocity contour at the systemic velocity, $v_{\rm sys}$, is also visibly bent. The major axis H I *pv* diagram in Fig. 18 is typical of a warped galaxy: superimposed on the typical two-component rotational behaviour of a late-type spiral, with solid-body rotation in its inner part and differential rotation further out, another component is visible in the *pv* diagram that goes from end to end, through the centre, in a straight line. More information on warps can be found, e.g., in García-Ruiz et al. (2002), Bottema (1995) and Brinks & Burton (1984).

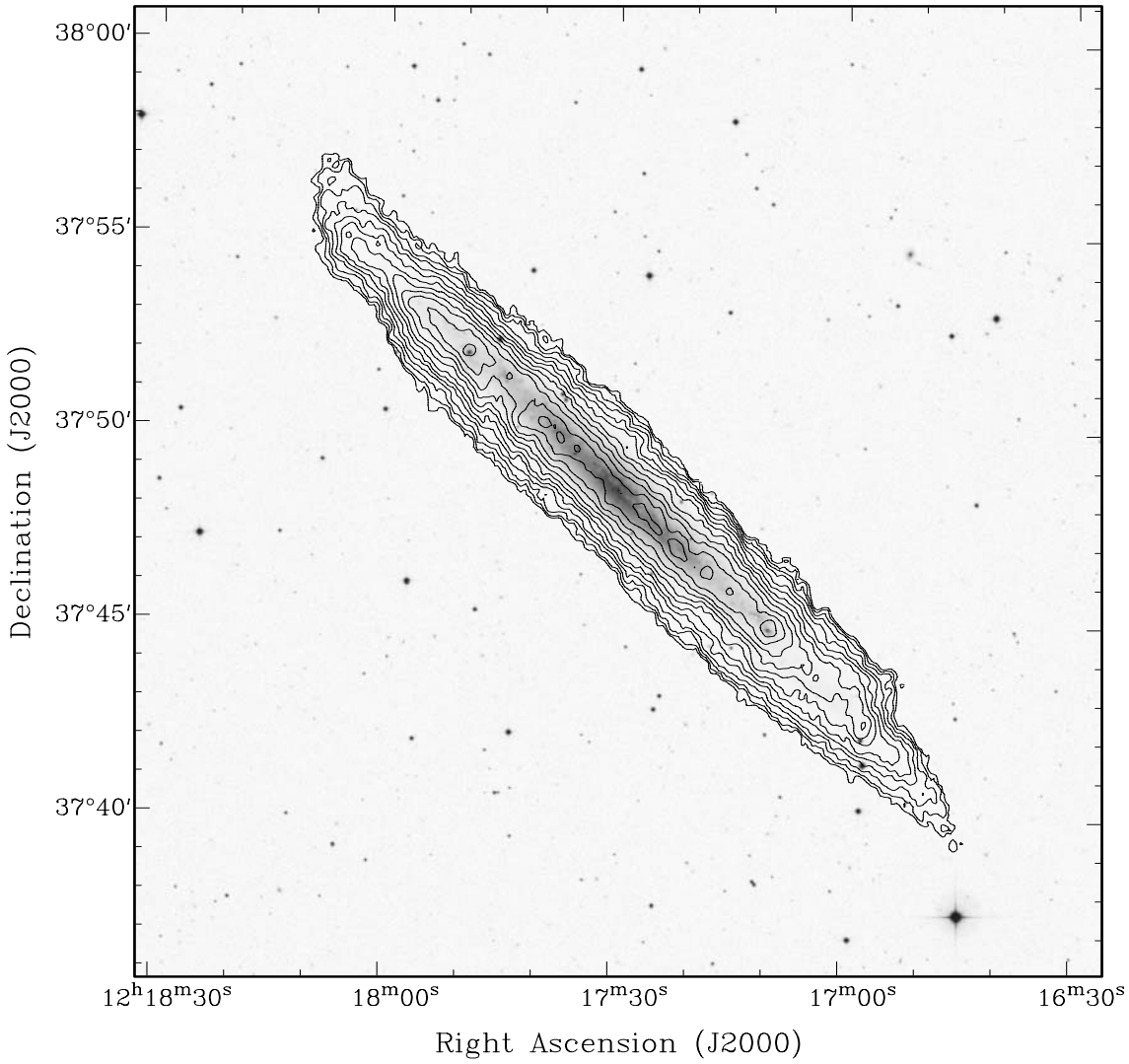

Fig. 11. NGC 4244 overlay of HI total intensity map on DSS-2 red optical image. The FOV is 25′ × 25′ (21.8 kpc × 21.8 kpc). Contours are at the 0.03 (=1.7 × 10^{20} cm^{-2}), 0.042, 0.06, ..., 1.344 Jy km s^{-1} surface brightness levels, separated by factors of $\sqrt{2}$.

Our results on NGC 4565 are in agreement with those presented by Rupen (1991).

NGC 4562, the south-eastern companion, exhibits regular rotation throughout its disk. There is no evidence of rotation in the velocity field of the northern companion, NGP9 F378-0021557 (for more information see Table 6 in Sect. 3.8.1).

3.5. NGC 4700

H I channel maps of NGC 4700 and a small partner to the south are displayed in Figs. 19 and 20. The distribution of H I emission from the disk plane of NGC 4700 is approximately symmetric, with a central depression and a maximum either side of the disk, the northeastern of which is stronger than its southwestern counterpart (Figs. 20 and 21). At both ends of the disk the H I distribution bends, which might indicate the presence of a warp. The H I distribution in NGC 4700 is thick (Figs. 20 and 21), indicating the tentative detection of gas beyond the disk plane of NGC 4700. The gas kinematics in the disk is regular (Figs. 22 and 23).

The possible presence of extraplanar H I in NGC 4700 is particularly interesting, because it is quite isolated; its nearest companion, 2MASX J12485413-1140424, which was detected in our observations (see below; Sect. 3.8.1, Table 6) is located at a projected distance of ca. 16′ (115 kpc for D = 25.5 Mpc) to the south (Fig. 19). This is roughly twice the distance between our Galaxy and the LMC, making a direct tidal disturbance by this companion at the present time quite unlikely.

An investigation into the nature of the extraplanar H I gas will require full three-dimensional modeling.

3.6. NGC 7090

The H I gas distribution in NGC 7090 is peculiar (see Figs. 24 and 25), in the sense that to the southeast of the centre it looks quite normal, possibly thick, while northwest of the central region NGC 7090 looks depleted of part of its neutral atomic gas. Both the optical appearance and the gas distribution are slightly

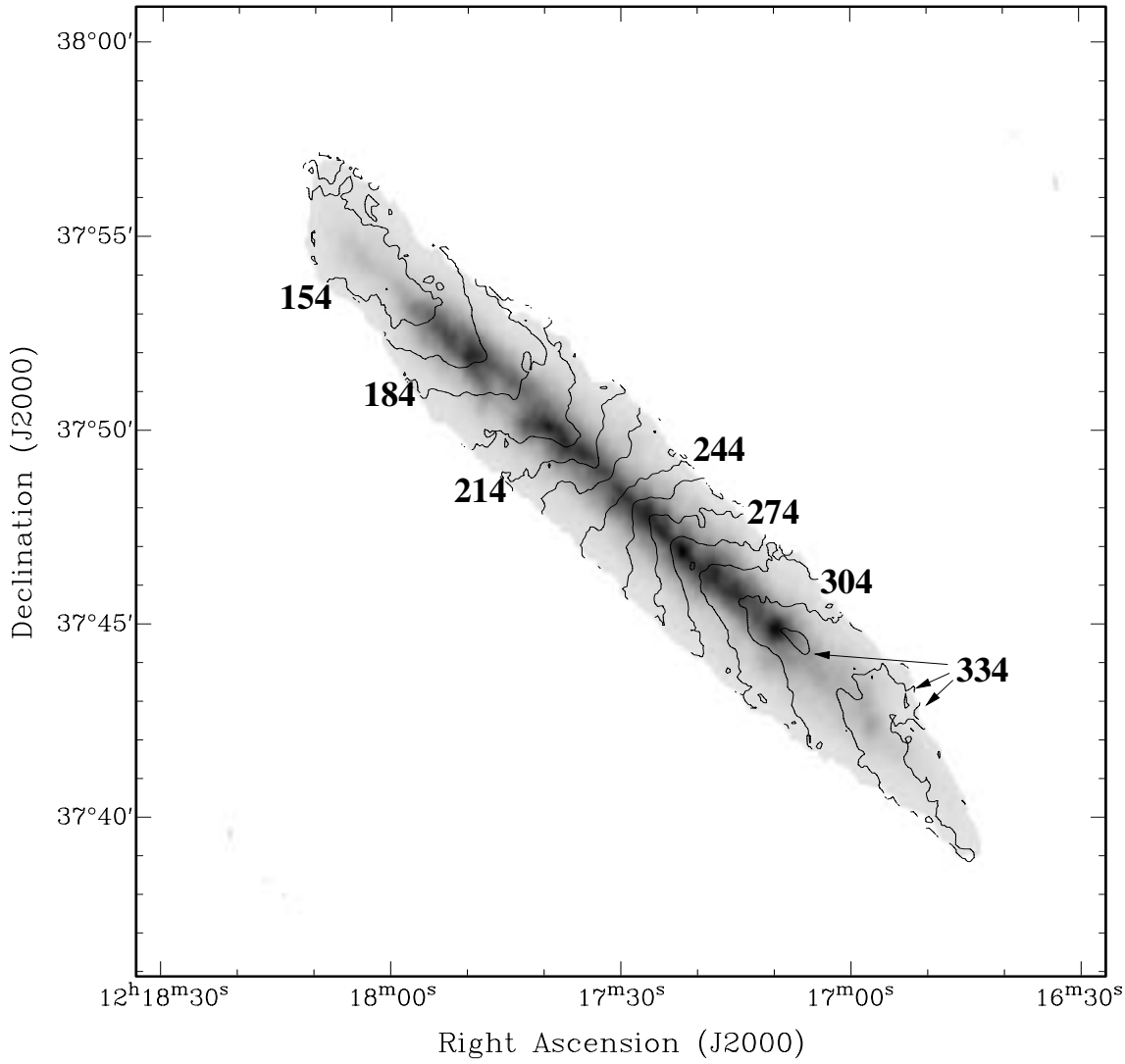

Fig. 12. NGC 4244 HI velocity field overlaid on HI total intensity image. The FOV is the same as in Fig. 11. The contours display the galaxy's systemic velocity of 244 km s^{-1} ± (n × 15) km s^{-1}, ranging from 154 km s^{-1} to 334 km s^{-1}.

disturbed, but there is no partner galaxy in sight that might have caused these peculiarities (Figs. 24 and 25). What is even more striking is that within the disk plane the H I gas in NGC 7090 is radially confined to within the optically visible galaxy disk, which is also asymmetric (Fig. 25). The asymmetry of the optical emission can be seen better in a DSS image without contours overlaid. There is no detected gas beyond the stellar disk down to the sensitivity limit of our data.

In addition to the gas distribution, the kinematics of NGC 7090 is also slightly disturbed, as can be seen in the velocity field (Fig. 26), and even more clearly in the *pv*-diagram along its major axis (Fig. 27). Detailed 3-D modeling of the datacube will be performed in due course to determine the cause of this peculiarity. Note that one can see an extended region with negative flux levels in the *pv*-diagram, which is caused by residual effects of Solar interference that could not be removed entirely from the data without losing information on extended H I emission at the same time. This should not affect the quantities derived here measurably, except for an increased uncertainty of the total H I line flux, which might be underestimated by of order 10%.

3.7. NGC 7462

Figures 28 and 29 show a very regular H I gas distribution in NGC 7462. However, the H I velocity field depicted in Fig. 30 exhibits some irregularities, as evidenced by the bend in the contour at systemic velocity (1064 km s^{-1}) and its not being at right angles with the galaxy's major axis. An asymmetry also shows in the major axis *pv* diagram in Fig. 31.

3.8. Summary of fitted HI disk properties

The observations presented here will be used to determine whether H I gas exists outside the disks of the target galaxies. To that end, three-dimensional modeling will be performed. However, some basic properties can be determined by other means. The following quantities were derived using the routine

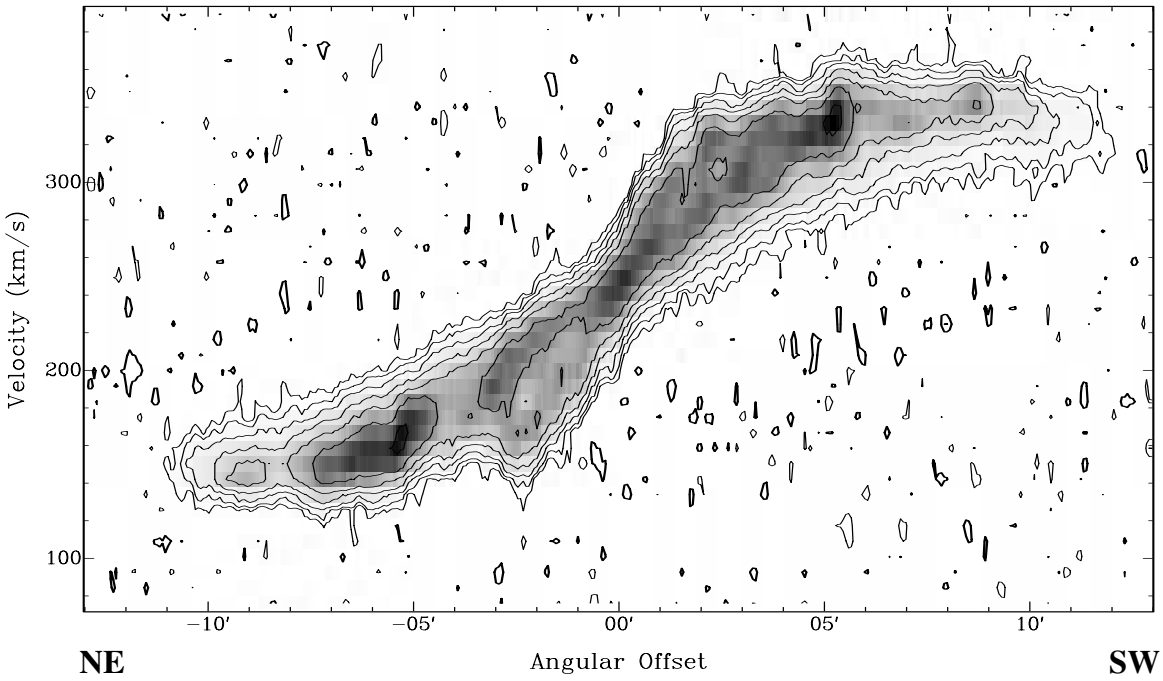

Fig. 13. NGC 4244 *pv* diagram along the major axis, covering a radial range of ±13′ (±11.3 kpc). Contours show surface brightness levels of −1.2, –0.6, 0.6 (=2.5-σ), 1.2, 2.4, ..., 38.4 mJy beam^{-1}, separated by factors of 2. Negative contours are bold.

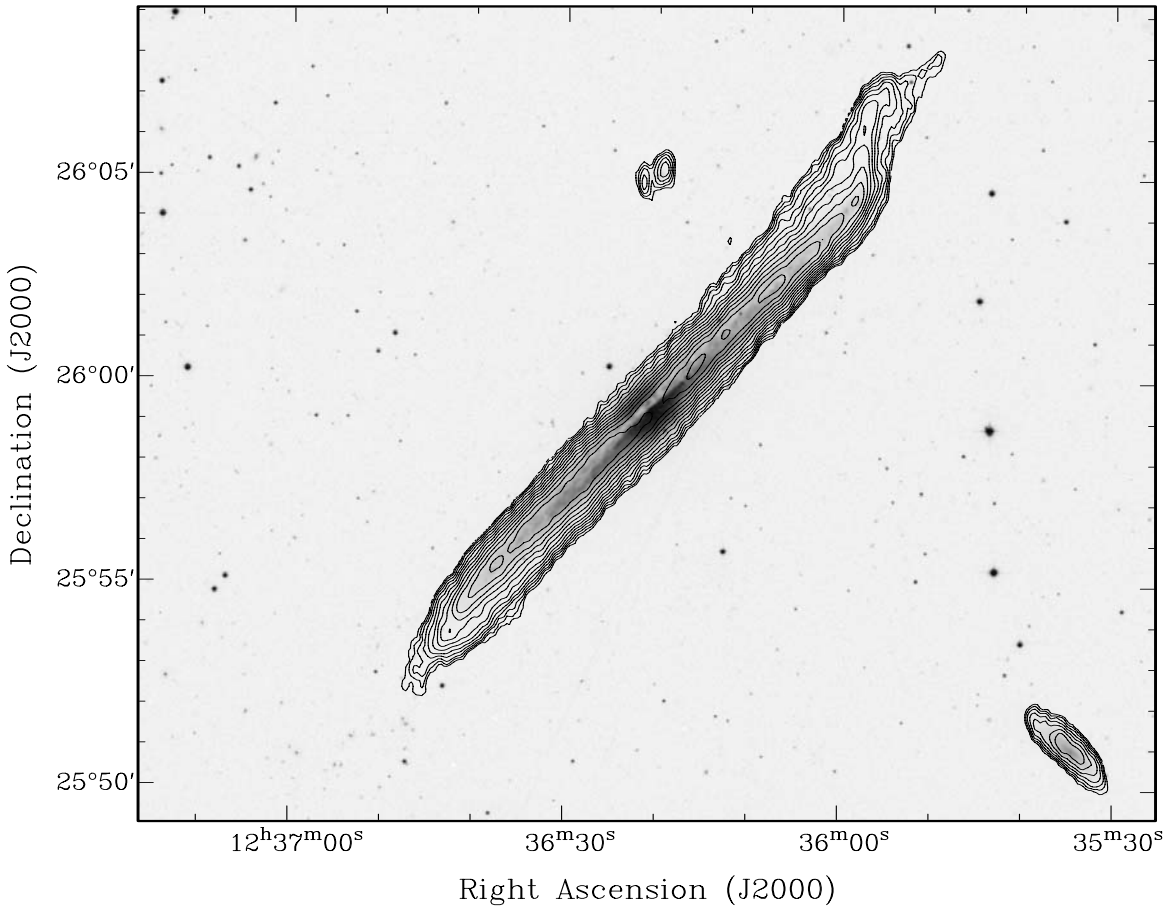

Fig. 16. NGC 4565 overlay of HI total intensity map on DSS-2 red optical image. The FOV is 25′ × 20′ (70.6 kpc × 56.5 kpc). Contours are at the 0.035 (=1.5 × 10^{20} cm^{-2}), 0.05, 0.07, ..., 2.24 Jy km s^{-1} surface brightness levels, separated by factors of $\sqrt{2}$.

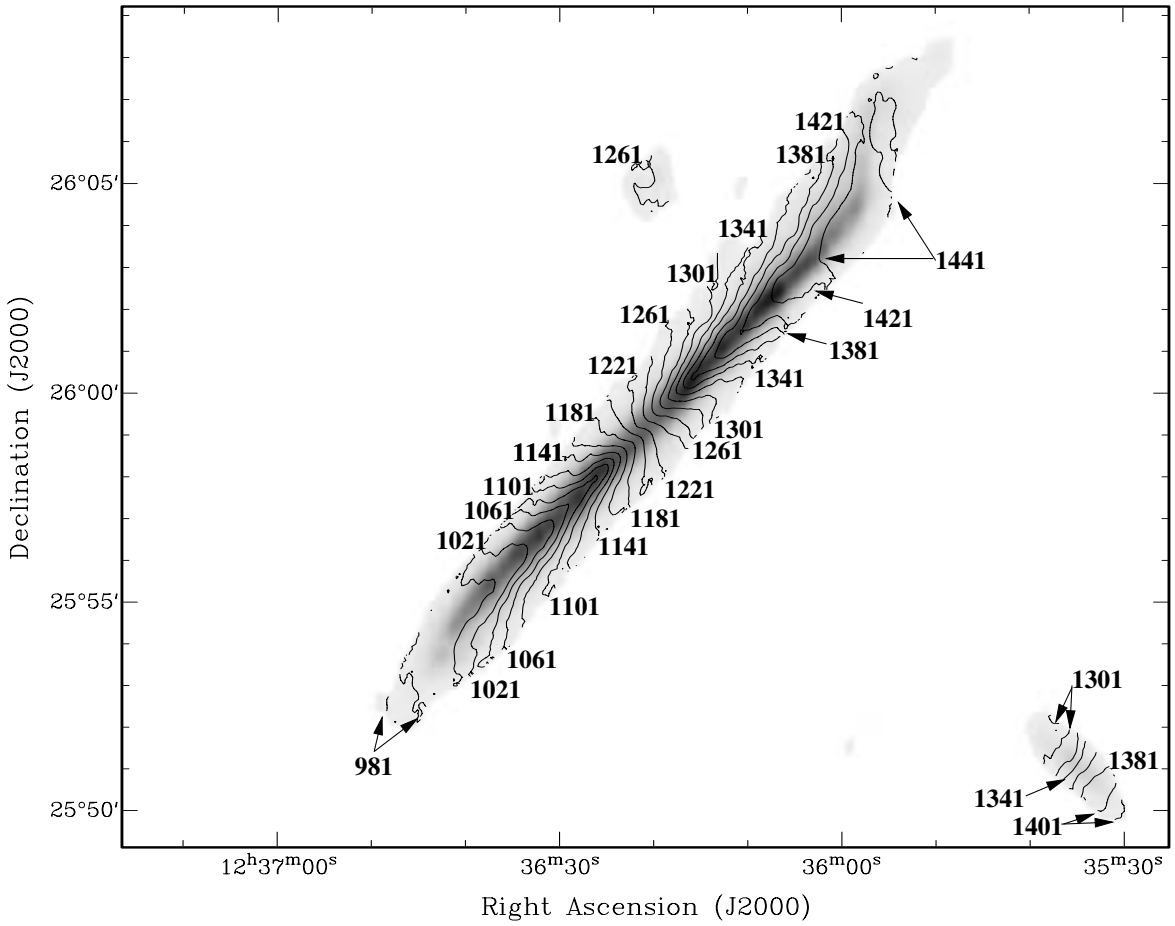

Fig. 17. HI velocity field of NGC 4565 and companions, overlaid on our HI total intensity image. The FOV is the same as in Fig. 16. The contours display the galaxy's systemic velocity of 1221 km s^{-1} ± (n × 20) km s^{-1}, ranging from 981 km s^{-1} to 1441 km s^{-1}.

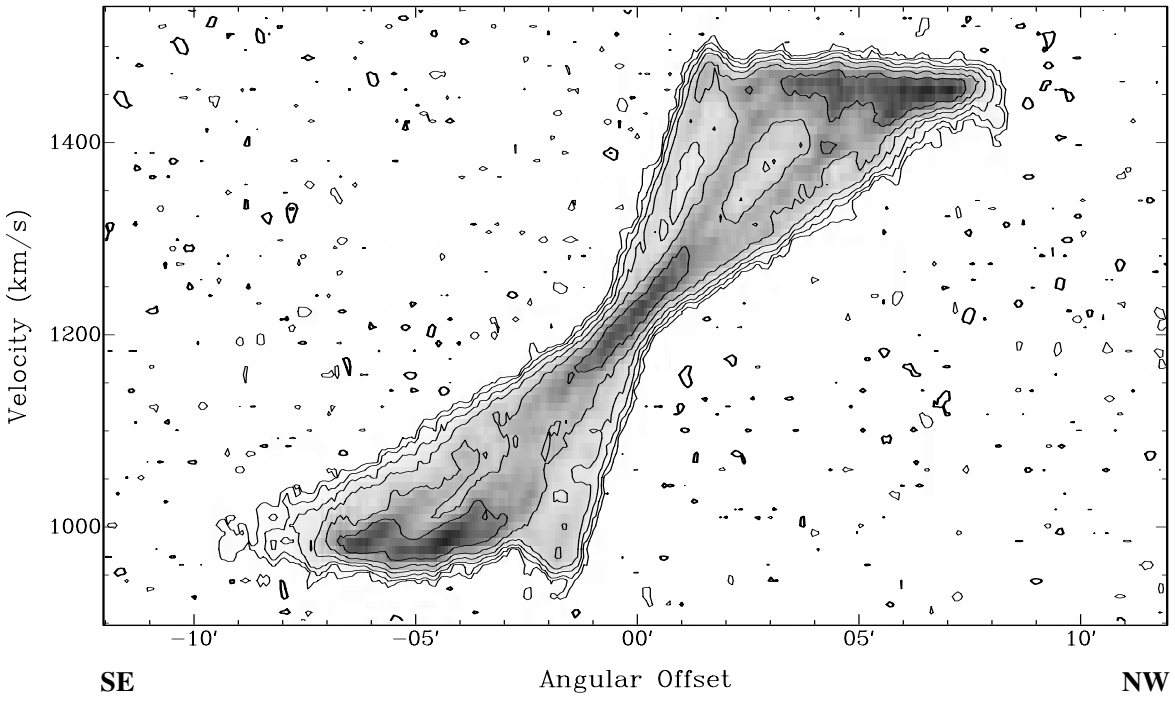

Fig. 18. NGC 4565 *pv* diagram along the major axis, covering a radial range of ±12′ (±33.9 kpc). Contours show surface brightness levels of −1.2, –0.6, 0.6 (=2.5-σ), 1.2, 2.4, ..., 19.2 mJy beam^{-1}, separated by factors of 2. Negative contours are bold.

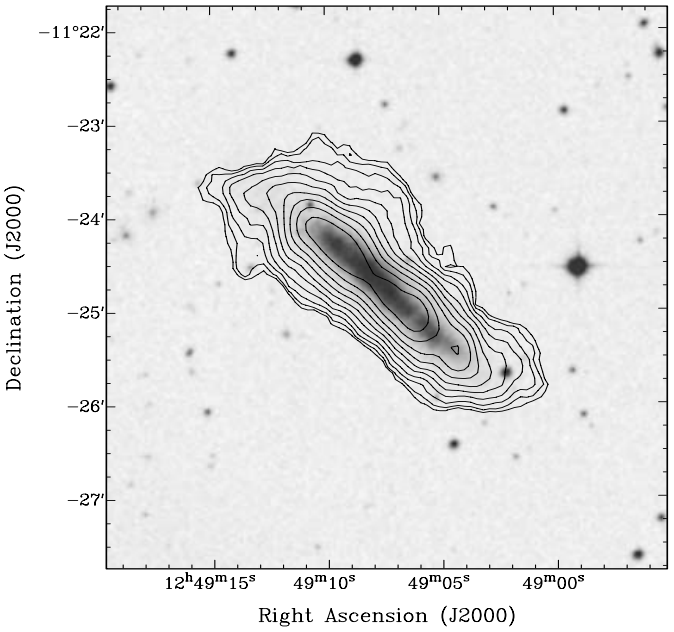

Fig. 21. NGC 4700 overlay of HI total intensity map on DSS-2 red optical image. The FOV is $6' \times 6'$ (44.5 kpc × 44.5 kpc). Contours are at the 0.05 (=1.9 × 10^{20} cm^{-2}), 0.07, 0.1, ..., 1.12 Jy km s^{-1} surface brightness levels, separated by factors of $\sqrt{2}$.

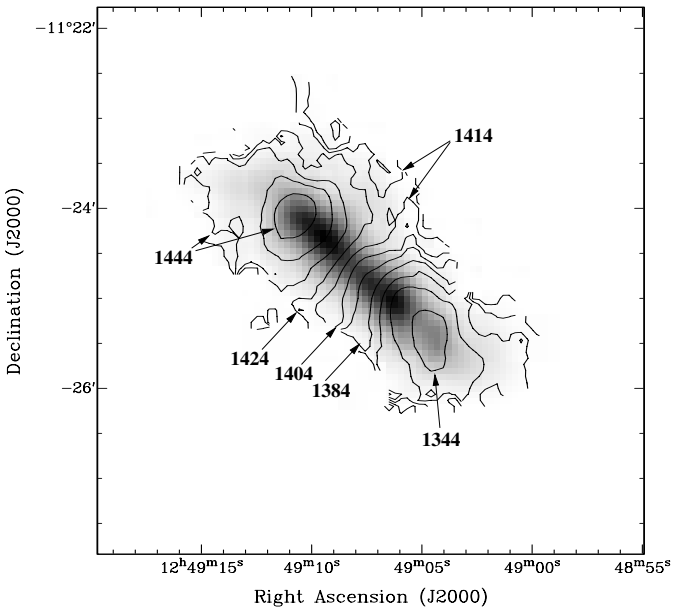

Fig. 22. NGC 4700 HI velocity field overlaid on HI total intensity image. The FOV is the same as in Fig. 21. The contours display the galaxy's systemic velocity of 1404 km s^{-1} ± (n × 10) km s^{-1}, ranging from 1344 km s^{-1} to 1444 km s^{-1}.

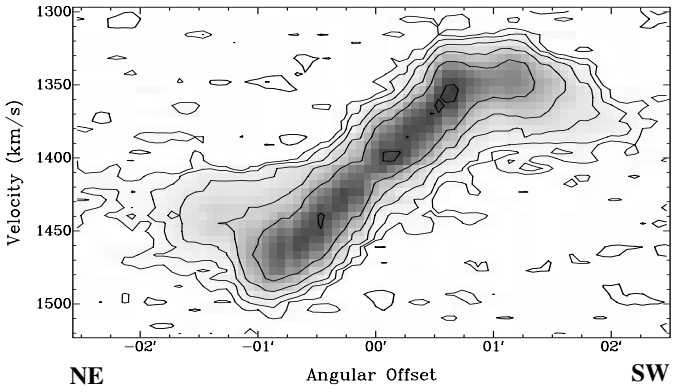

Fig. 23. NGC 4700 *pv* diagram along the major axis, covering a radial range of ±2.′5 (±18.6 kpc). Contours show surface brightness levels of −1.8, –0.9, 0.9 (=2.5-σ), 1.8, 3.6, ... 28.8 mJy beam^{-1}, separated by factors of 2. Negative contours are bold.

ROTCUR in the GIPSY software package[4], which fits tilted-ring models to the data:

α, δ(2000) = *kinematic* centre position,
$v_{\rm hel}$ = heliocentric system recession velocity,
PA = position angle (counter-clockwise from north).

For the fits we used a step size of 10″, which corresponds to roughly half a beamwidth.

$v_{\rm max}$, the maximum mean rotation velocity, and R_0, the radius at which the maximum rotation velocity is reached, were determined from the *pv* diagrams. Based on inclination angles from the literature, the deprojected maximum rotation velocity, $v^{\rm i}_{\rm max}$, was calculated. In addition, the total H I line flux, $f_{\rm HI}$, was used to measure the total atomic gas mass, $M_{\rm atom}$, (with a 35% correction for helium). Table 5 summarises these results. If not mentioned otherwise, the uncertainties of the fit parameters are about 3″–5″ for all positions, 2–3 km s^{-1} for all velocities and 2°–3° for PA. The inclination angles from Tully (1988) have a larger uncertainty of up to 5°.

The fit to the velocity field of NGC 1406 does not include the disturbed northern part of the disk. The PA values are constant to within the measurement accuracy across the disk.

The best-fitting PA of NGC 1511 changes from about 290° to 300°, with a mean value of 295° (Table 5) from the centre to a radius of about 2′.

The best-fitting PA of NGC 4244 is 225° in the central disk and changes steadily towards 228° at a galactocentric distance, r, of 10′ (8.7 kpc).

In the disk of NGC 4565 the best-fitting PA slopes from 320° in the central 1.′5 to 312° at r = 7′ (14.3 kpc).

The kinematic behaviour of NGC 4666 was described by Walter et al. (2004). Both PA and i change at the outer edge of the optically visible galaxy disk, where the H I gas starts to warp out of the disk plane.

The PA measurements are almost constant across the disk of NGC 4700.

The PA measurements at various radii in the disk of NGC 7090 show no significant trends with galactocentric distance, despite the asymmetries mentioned above.

The fits to the velocity field of NGC 7462 show no significant trend of the PA with radial distance from the galaxy centre.

[4] The Groningen Image Processing System; van der Hulst et al. (1992).

Table 5. General H I properties.

	NGC 1406	NGC 1511	NGC 4244	NGC 4565	NGC 4666[a]	NGC 4700	NGC 7090	NGC 7462
α(2000)[b]	03:39:22.8	03:59:36.9	12:17:29.9	12:36:21.0	12:45:08.3	12:49:07.6	21:36:28.6	23:02:46.5
δ(2000)[b]	–31:19:16	–67:38:08	+37:48:31	+25:59:13	–00:27:51	–11:24:47	–54:33:24	–40:50:05
D (Mpc)[c]	14.9	17.5	3.0	9.7[d]	26.4	25.5	11.7	15.1
$v_{\rm hel}$ (km s^{-1})	1051	1335	244	1221	1520	1404	849	1064
PA (°)	199	295	228	315	225	48	130	253
i (°)	90[e]	72[e]	84.5[f]	≥87.5[g]	70	90[e]	90[e]	90[e]
$v_{\rm max}$ (km s^{-1})	171	150	113	271	180	87	124	112
$v^{\rm i}_{\rm max}$ (km s^{-1})	171	158	114	271	192	87	124	112
R_0 (kpc)	4.1	4.9	4.7	4.8	17	5.6	5.7	4.5
$f_{\rm HI}$ (Jy km s^{-1})	62.3	44.3	379	249	93.5	21.7	39.8	32.7
$M_{\rm atom}$ (10^9 $M_\odot$)	4.40	4.32	1.09	7.45	15.3	4.48	1.73	2.37

Notes (for details see text):
[a] Values from Walter et al. (2004).
[b] The kinematic centre positions were determined from rotation curve fitting using routine ROTCUR in GIPSY (see text).
[c] Distances are based on H_0 = 75 Mpc km s^{-1} and a virgocentric infall velocity of 300 km s^{-1} (cf. Dahlem et al. 2001).
[d] The distance of NGC 4565 is hard to determine because of the peculiar velocities of the Coma clouds (Ferrarese et al. 2000). The value used here is from Tully (1988).
[e] Tully (1988).
[f] Olling (1996a).
[g] Rupen (1991).

Table 6. General H I properties of companion galaxies.

	NGC 1511a	NGC 1511b	NGC 4562	NGP9 F378-0021557	2MASX J12485413-1140424
α(2000)	04:00:17.9	04:00:53.2	12:35:34.8	12:36:20.2	12:48:54.2
δ(2000)	–67:48:26	–67:36:38	+25:51:09	+26:04:59	–11:40:32
D (Mpc)[a]	17.5	17.5	9.7	9.7	25.5
$v_{\rm hel}$ (km s^{-1})	1339 ± 5	1420 ± 10	1347	1260 ± 5	1329 ± 5
$v_{\rm max}$ (km s^{-1})	55 ± 10	27	33	–	–
i (°)	–	81	86	–	–
PA (°)	268	85	121	–	0 ± 5
$f_{\rm HI}$ (Jy km s^{-1})	2.91	4.79	5.34	0.91	3.10
$M_{\rm atom}$ (10^9 $M_\odot$)	0.28	0.47	0.16	0.027	0.64

Notes:
[a] Distances are based on H_0 = 75 Mpc km s^{-1} and a virgocentric infall velocity of 300 km s^{-1} (cf. Dahlem et al. 2001). They are assumed here to be the same as those of the dominant galaxies in the respective groups (Table 5).

3.8.1. HI properties of companion galaxies

Although visibly causing gas disturbances only in the case of NGC 1511, partner galaxies were detected in three of the seven observations presented here, near NGC 1511, NGC 4565 and NGC 4700 (and previously also near NGC 4666, for a description see Walter et al. 2004). The properties of those detected around the present sample of 7 galaxies are collated in Table 6. "–" mark properties that could not be determined reliably. These serendipitous detections will not be discussed any further here.

4. Discussion

The new H I observations presented above were obtained with the goal of searching, with a limiting sensitivity in column densities of order a few times 10^{19} cm^{-2}, for low surface brightness gas around the sample galaxies. In addition to H I in the disks of the target galaxies we have found the following types of H I gas.

4.1. Previously unknown interaction partners

Including the previously published results on NGC 4666, our observations reveal the presence of small companions around 4 out of 8 galaxies in the present sample. Although visible in the DSS, the small galaxies near NGC 4666 and NGC 4700 were not previously known to be physical partners and in the case of NGC 1511 not known to be currently tidally interacting. Our data of NGC 4565 and its companions allow for a more detailed analysis than previous, less sensitive observations (Rupen 1991).

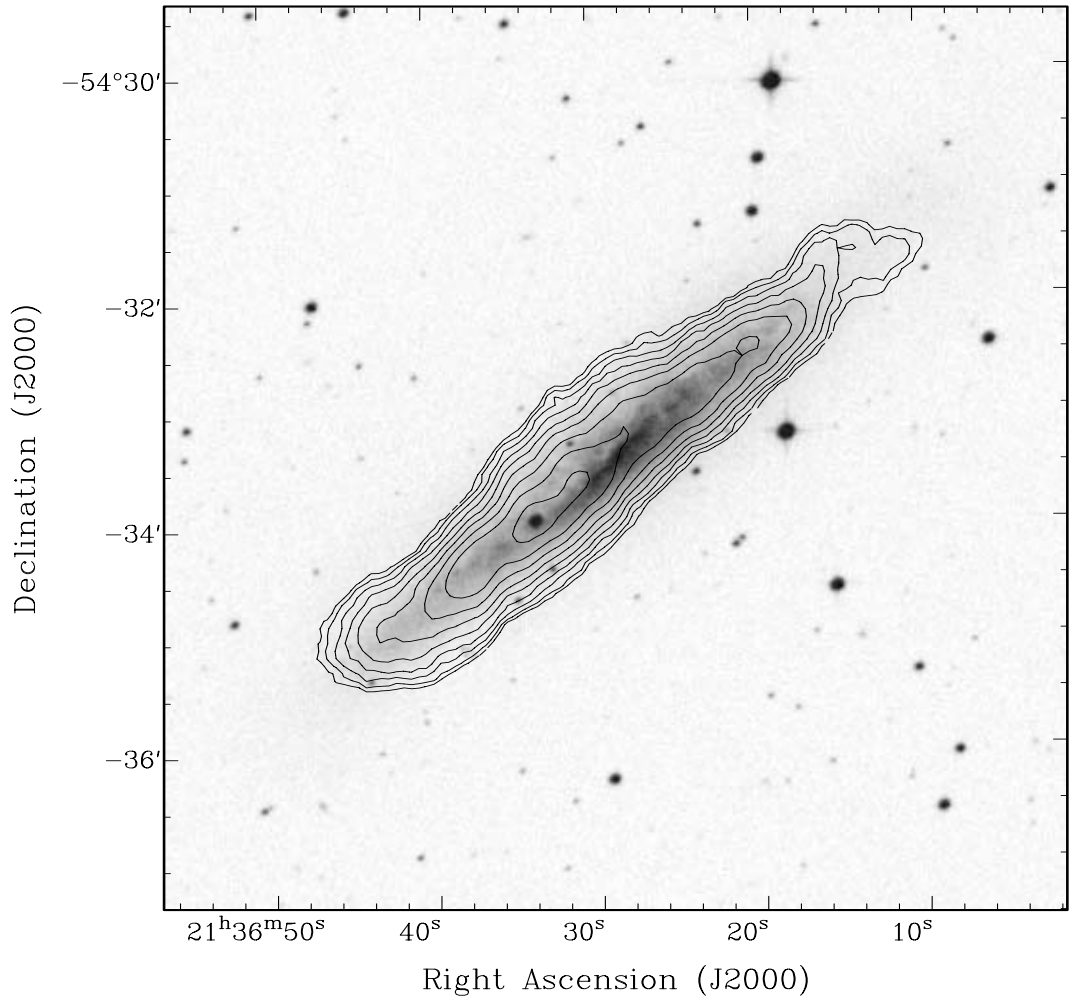

Fig. 25. NGC 7090 overlay of HI total intensity map on DSS-2 red optical image. The FOV is $8' \times 8'$ (27.5 kpc × 27.5 kpc). Contours are at the 0.10 (=3.8×10^{20} cm^{-2}), 0.14, 0.2, ..., 1.6 Jy km s^{-1} surface brightness levels, separated by factors of $\sqrt{2}$.

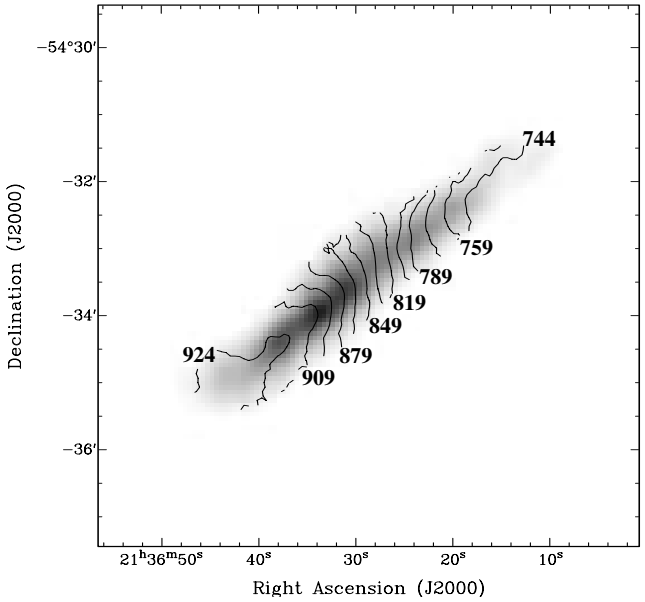

Fig. 26. NGC 7090 HI velocity field overlaid on HI total intensity image. The FOV is the same as in Fig. 25. The contours display the galaxy's systemic velocity of 849 km s^{-1} ± ($n \times 15$) km s^{-1}, ranging from 744 km s^{-1} to 924 km s^{-1}.

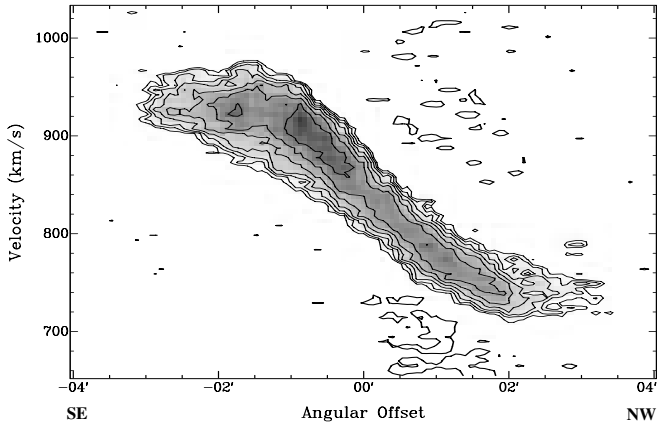

Fig. 27. NGC 7090 *pv* diagram along the major axis, covering a radial range of ±4′ (±13.6 kpc). Contours show surface brightness levels of −4.0, −2.8, 2.8 (=2.5-σ), 4.0, 5.6, ... 22.4 mJy beam^{-1}, separated by factors of $\sqrt{2}$. Negative contours are bold.

4.2. Tidal features

The plumes and tails found around NGC 1511 and NGC 4666 were not previously known to exist. As mentioned by

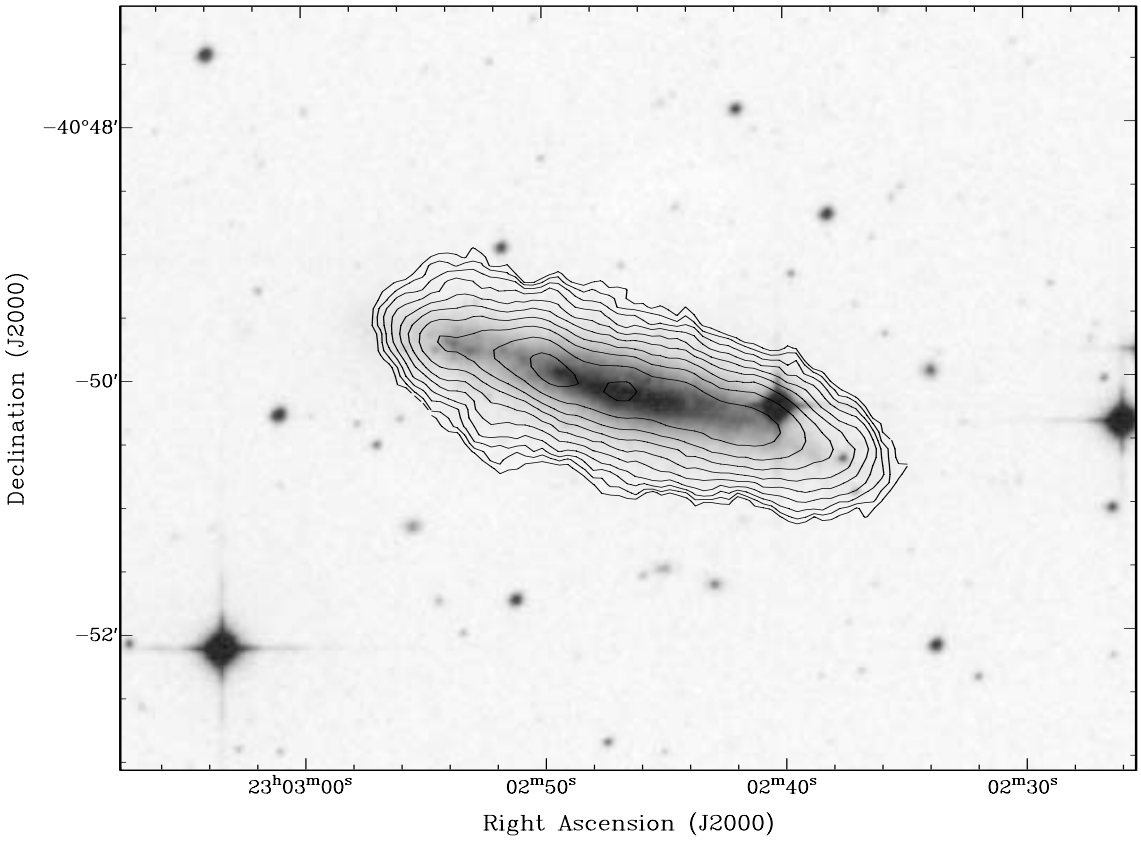

Fig. 29. NGC 7462 overlay of HI total intensity map on DSS-2 red optical image. The FOV is $8' \times 6'$ (35.2 kpc × 26.4 kpc). Contours are at the 0.075 (=2.9×10^{20} cm^{-2}), 0.106, 0.15, ..., 1.68 Jy km s^{-1} surface brightness levels, separated by factors of $\sqrt{2}$.

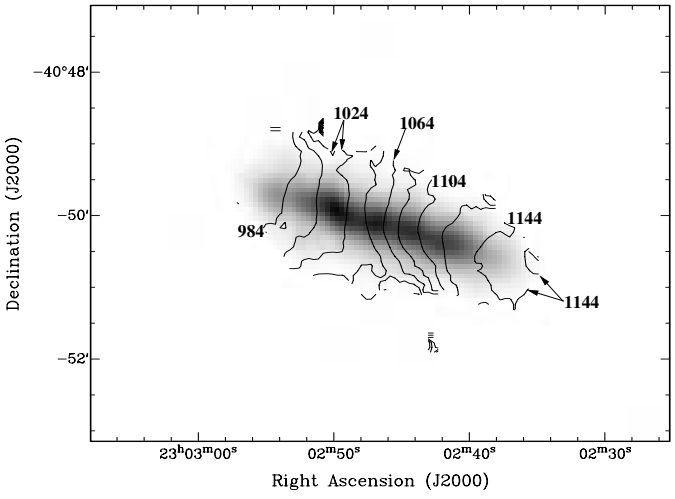

Fig. 30. NGC 7462 HI velocity field overlaid on HI total intensity image. The FOV is the same as in Fig. 29. The contours display the galaxy's systemic velocity of 1064 km s^{-1} ± ($n \times 20$) km s^{-1}, ranging from 984 km s^{-1} to 1144 km s^{-1}.

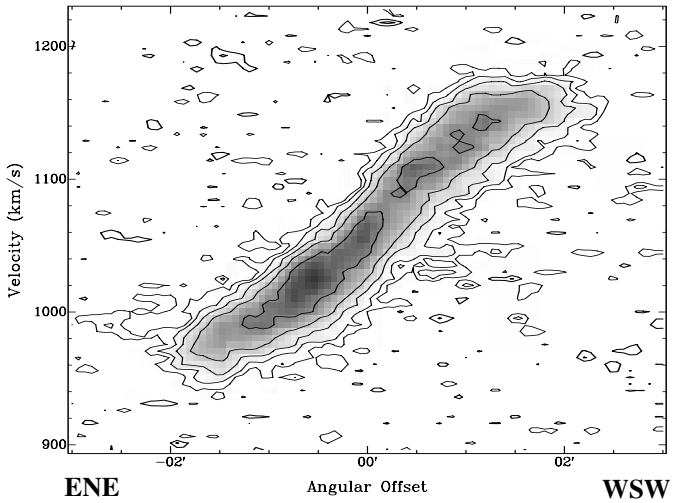

Fig. 31. NGC 7462 *pv* diagram along the major axis, covering a radial range of ±3′ (±13.2 kpc). Contours show surface brightness levels of –3, –1.5, 1.5 (=2.5-σ), 3, 6, 12, 24 mJy beam^{-1}, separated by factors of 2. Negative contours are bold.

Walter et al. (2004), the tidal gas increases the cross section of neutral gas for radiation coming from higher redshift objects located behind the interacting groups, making them possible candidates for near-zero redshift Lyman-α absorbers.

The warp in NGC 4565 was previously reported (Rupen 1991), while the one in NGC 1406 was detected for the first time in our observations.

4.3. Absence of candidate primordial HI gas clouds

None of our high-sensitivity datasets reveal the presence of H I gas without an optical counterpart on a DSS-2 plate, thus contradicting the theory that large numbers of low-mass primordial gas clouds might constitute a reservoir for high-velocity gas clouds raining down on galaxy disks (Oort 1966;

Blitz et al. 1999). With the sensitivity of our data we should pick up at least the upper end of the expected mass distribution of such clouds of order 10^7 $M_\odot$ (cf. Walter et al. 2004).

4.4. Extraplanar neutral hydrogen gas

Our data enable us to search for extraplanar gas in a small sample of edge-on galaxies, with a sensitivity similar to that of the NGC 891 data by Swaters et al. (1997). The results outlined above describe the distribution and kinematics of H I gas in the galaxy disks. These global parameters describe mostly what must be considered the "normal" behaviour of the target galaxies. The salient disk properties will be used to constrain the properties of H I model cubes.

The analysis of the vertical gas distribution in a search for extraplanar H I gas and other searches for deviations from this "normal" behaviour are underway and will be presented in due course.

A by-eye inspection of our data reveals that only NGC 4700 exhibits signs of extraplanar atomic hydrogen gas. For all other objects a more quantitative analysis is required.

It is found from the present analysis that NGC 1511 is not a good candidate for a search of extraplanar H I gas in SF-related gaseous outflows from its disk due to the obvious, dominant large-scale disturbances caused by its partners. Instead, the system appears to be suitable for n-body simulations, similar to the work done previously on the Leo triplet (Haynes et al. 1979) and the NGC 4631 group of galaxies (Combes 1978), amongst others, to study the tidal interaction with its partners.

NGC 4565 will not be excluded from our sample, because possibly only part of its disk is disturbed by the influence of its two dwarf companions. The remainder of its disk can be used for a search of extraplanar gas that was not transported out of the disk by a companion's gravitational drag.

In the case of NGC 4700 the partner is at such a large projected distance that it is unlikely to have a direct influence on its H I distribution.

Acknowledgements. We thank F. Walter for comments on a draft version of this paper. Many thanks to the ATNF staff, especially R. Sault and M. Wieringa, for their help with the ATCA data reduction; to the ASTRON staff, in particular T. Oosterloo, for the help received with the WSRT observations; and to M. Rupen and the VLA analysts for their support during the VLA observations and data reduction. We thank H. Terlouw, J. M. van der Hulst and E. de Blok for their help with the GIPSY package. We are grateful to an anonymous referee for very helpful, positive criticism. This research has made use of the NASA Extragalactic Database (NED), whose contributions to this paper are gratefully acknowledged. The Digitized Sky Survey was produced at the Space Telescope Science Institute under US Government grant NAG W-2166. The National Geographic Society – Palomar Observatory Sky Atlas (POSS-I) was made by the California Institute of Technology with grants from the National Geographic Society.

References

Barnes, D. G., Staveley-Smith, L., de Blok, W. J. G., et al. 2001, MNRAS, 322, 486
Blitz, L., Spergel, D. N., Teuben, P. J., Hartmann, D., & Burton, W. B. 1999, ApJ, 514, 818
Boomsma, R., Oosterloo, T. A., Fraternali F., van der Hulst, J. M., & Sancisi, R. 2005, A&A, 431, 65
Bottema, R. 1995, A&A, 295, 605
Brinks, E., & Burton, W. B. 1984, A&A, 141, 195
Combes, F. 1978, A&A, 65, 47
Dahlem, M., Lazendic, J. S., Haynes, R. F., Ehle, M., & Lisenfeld, U. 2001, A&A, 374, 42
Ekers, R. D., & Sancisi, R. 1977, A&A, 54, 973
Ferrarese, L., Ford, H. C., Huchra, J., et al. 2000, ApJS, 128, 431
Fraternali, F., van Moorsel, G., Sancisi, R., & Oosterloo, T. 2002, AJ, 123, 3124
Fraternali, F. 2003, IAU Symp., 217, 44
Fraternali, F., Oosterloo, T., & Sancisi, R. 2004, Ap&SS, 289, 377
García-Ruiz, I., Sancisi, R., & Kuijken, K. 2002, A&A, 394, 769
Haynes, M. P., Giovanelli, R., & Roberts, M. S. 1979, ApJ, 229, 83
van der Hulst, J. M. 2004, in Extra-planar Gas, conference held at Astron, Dwingeloo, 7−11 June 2004, ASP Conf. Ser. (in Prep.)
van der Hulst, J. M., Terlouw, J. P., Begeman, K., Zwitser, W., & Roelfsema, P. R. 1992, The Groningen Image Processing System, GIPSY, in Astronomical Data Analysis Software and Systems I, ed. D. M. Worall, C. Biemesderfer, & J. Barnes, ASP Conf. Ser., 25, 131
Irwin, J. A., & Chaves, T. 2003, ApJ, 585, 268
Jones, K. L., Koribalski, B., Elmouttie, M., & Haynes, R. F. 1999, MNRAS, 302, 649
Kalberla, P. M. W., Westphalen, G., Mebold, U., Hartmann, D., & Burton, W. B. 1998, A&A, 332, L61
Kamphuis, J., & Briggs, F. 1992, A&A, 253, 335
Kraus, J. D., & Dixon, R. S. 1967, AJ, 72, 809
Mathewson, D. S., Ford, V. L., & Buchhorn, M. 1992, ApJS, 81, 413
Matthews, L. D., & Wood, K. 2003, ApJ, 593, 721
Meyer, M. J., Zwaan, M. A., Webster, R. L., et al. 2004, MNRAS, 350, 1195
Olling, R. P. 1996a, AJ, 112, 457
Olling, R. P. 1996b, AJ, 112, 481
Oort, J. H. 1966, Bull. Astron. Inst. Netherlands, 18, 421
Rand, R. J., & Stone, J. M. 1996, AJ, 111, 190
Rupen, M. P. 1991, AJ, 102, 48
Swaters, R. A., Sancisi, R., & van der Hulst, J. M. 1997, ApJ, 491, 140
Swaters, R. A., van Albada, T. S., van der Hulst, J. M., & Sancisi, R. 2002a, A&A, 390, 829
Swaters, R. A., & Balcells, M. 2002b, A&A, 390, 863
Tully, R. B. 1988, Nearby Galaxies Catalog (Cambridge University Press)
Walter, F., Dahlem, M., & Lisenfeld, U. 2004, ApJ, 606, 258
Wilding, T., Alexander, P., & Green, D. A. 1993, MNRAS, 263, 1075

Online Material

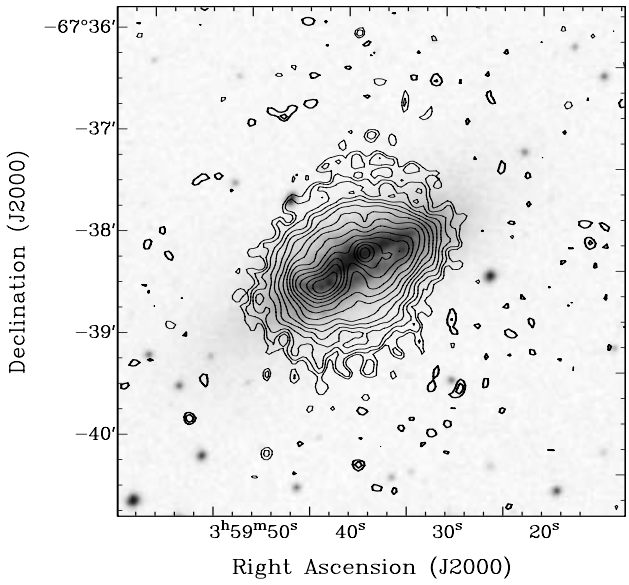

Fig. A.1. ATCA 1.38 GHz radio continuum image of NGC 1511, superimposed on a red DSS-2 optical plate. The contour levels are −0.092, –0.065, 0.065 (=2.5-σ), 0.092, 0.13, ..., 8 mJy beam^{-1}, spaced by factors of $\sqrt{2}$.

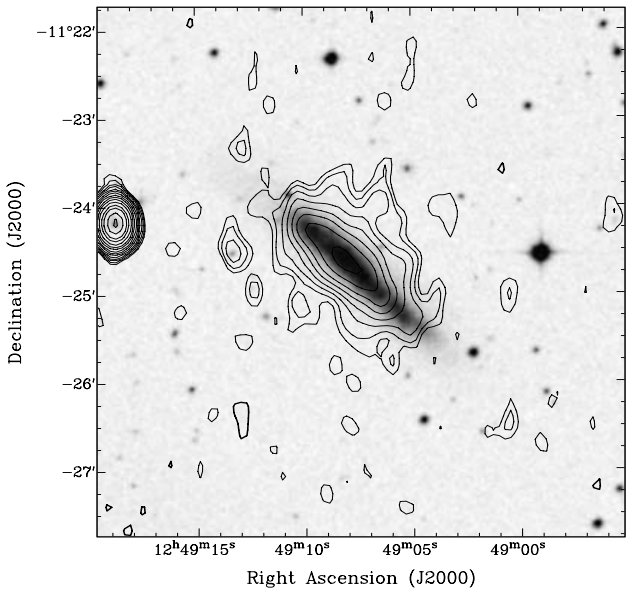

Fig. A.2. Narrow-band VLA 1.4 GHz total intensity radio continuum image of NGC 4700, superimposed on a red DSS-2 optical plate. The contour levels are –0.25, 0.25 (=2.5-σ), 0.35, 0.5, ... 32 mJy beam^{-1}, spaced by factors of $\sqrt{2}$.

Appendix A: New 1.4 GHz radio continuum images

Most of the continuum images obtained, either in parallel with our H I line observations or from the line-free channels, are not better than previously published data. However, in a few cases our 1.4 GHz radio continuum images contain new information. These are presented here.

A.1. 1.38 GHz radio continuum image of NGC 1511

With a beam of 5.″8 × 5.″3, our new 1.38 GHz image of NGC 1511 has a much higher resolution than the one published by us earlier (Dahlem et al. 2001). At the same time the new image has a much improved sensitivity of 28 μJy beam^{-1} (Fig. A.1). It exhibits the existence of two distinct radio continuum emission maxima in the galaxy disk, with a pronounced gap in between. The total emission distribution is almost circular, with a lot of emission arising from outside the optically visible disk, as discussed by us earlier.

A.2. 1.4 GHz radio continuum image of NGC 4700

The VLA 1.4 GHz continuum image of NGC 4700 from the line-free channels exhibits with much better angular resolution (20″ × 15″) than our earlier image (Dahlem et al. 2001) radio continuum emission from the galaxy halo (Fig. A.2). This separates the low surface brightness emission from nearby point sources which were confusing the earlier low-resolution image. More sensitive, wideband continuum observations with the VLA CnB configurations have been obtained, to be combined with our earlier D array observations. These will be presented in due course.

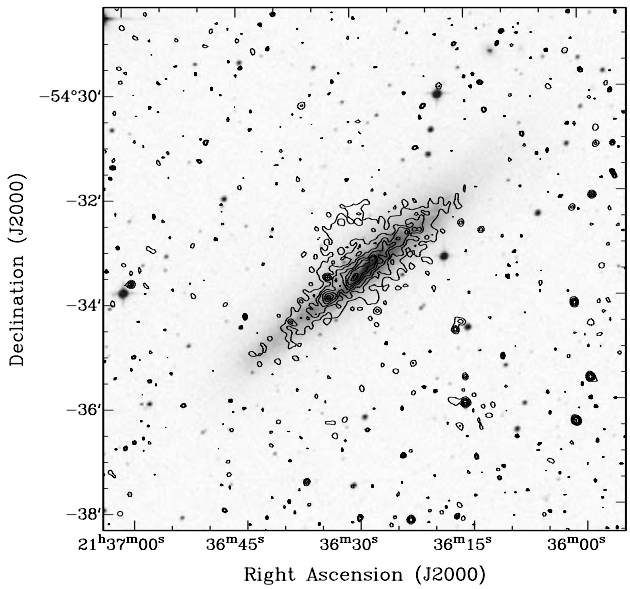

Fig. A.3. ATCA 1.38 GHz radio continuum image of NGC 7090, superimposed on a red DSS-2 optical plate. The contour levels are −0.084, –0.06, 0.06 (=2.5-σ), 0.084, 0.12, ... 2 mJy beam^{-1}, spaced by factors of $\sqrt{2}$.

A.3. 1.38 GHz radio continuum image of NGC 7090

The new 1.38 GHz continuum image of NGC 7090 obtained in parallel with our ATCA H I line observations is presented in Fig. A.3. The improved angular resolution of this image of 5.″8 × 5.″3 provides a much more detailed view of the radio continuum emission distribution, especially in the galaxy disk, while part of the radio halo is resolved out. The 1-σ point source sensitivity is 24 μJy beam^{-1}.

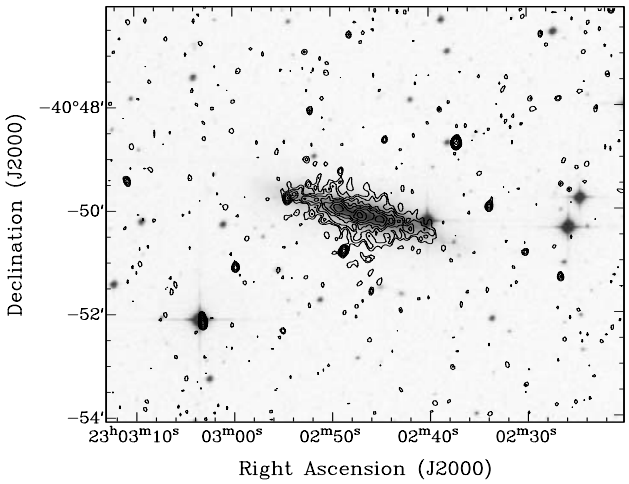

Fig. A.4. ATCA 1.38 GHz radio continuum image of NGC 7462, superimposed on a red DSS-2 optical plate. The contour levels are –0.06, 0.06 (=2.5-σ), 0.084, 0.12, ... 2 mJy beam^{-1}, spaced by factors of $\sqrt{2}$.

A.4. 1.38 GHz radio continuum image of NGC 7462

The new 1.38 GHz continuum image of NGC 7462 obtained in parallel with our ATCA H I line observations is presented in Fig. A.4). The improved angular resolution of this image of $7\farcs3 \times 5\farcs3$ provides a much more detailed view of the radio continuum emission distribution. At the same time the sensitivity of 23.5 μJy beam^{-1} is also much better than that of the old data (Dahlem et al. 2001).